Materials Today Communications 36 (2023) 106846

Contents lists available at ScienceDirect

Materials Today Communications

journal homepage: www.elsevier.com/locate/mtcomm

Exploring the performance of perovskite solar cells with dual hole transport layers via SCAPS-1D simulation

Biplav Dahal, Melorina Dolafi Rezaee, Ram Chandra Gotame, Wenzhi Li *

Department of Physics, Florida International University, Miami, FL 33199, USA

ARTICLE INFO

Keywords:
Perovskite solar cells
SCAPS-1D simulation
Inorganic HTL
Dual HTL
Spiro-OMeTAD
CZTS

ABSTRACT

The potential of perovskite solar cells (PSCs) to produce high efficiency (over 25 %) is well known, but the poor stability of these solar cells is still a concern for practical applications. Thus, improving the stability is essential for furthering the development of PSCs. To address this issue, researchers found that incorporating inorganic materials into the hole transport layers (HTLs) can improve the stability of PSCs, yet charge recombination at the interface between the perovskite and inorganic HTLs can still reduce the efficiency of the PSCs. This study simulated the performance and mechanism of methyl ammonium lead iodide ($MAPbI_3$) PSCs with a dual HTL using Solar Cell Capacitance Simulator-one Dimension (SCAPS-1D). A dual HTL formed by combining Spiro-OMeTAD (spiro), a highly efficient hole transport material, and copper zinc tin sulfide (CZTS), a highly stable hole transport material, leads to a PSC with a power conversion efficiency (PCE) of 23.47 % and significantly improved stability. Simulation results of the electric field at the interfaces of PSCs indicated that the PSC with spiro/CZTS as dual HTL have enhanced charge separation and reduced recombination. Furthermore, the simulation results have also revealed the influence of different parameters, such as absorber thickness, absorber defect density, HTL thickness, HTL/absorber interface defects, temperature, series resistance, and shunt resistance, on solar cell's characteristics.

1. Introduction

Pursuing a clean and sustainable energy future has increased interest in renewable energy sources, with photovoltaic technologies in the spotlight. Perovskite solar cells (PSCs) have emerged as a viable alternative to traditional silicon-based cells due to their high efficiency, low cost, and scalability potential. The impressive photovoltaic performance of PSCs is attributed to their remarkable optoelectronic properties, optimized energy band alignment, and finely attuned interface properties [1–4]. However, the long-term stability of PSCs is a concern, as they degrade more quickly than traditional cells, meaning that they need to be replaced more often. The performance of PSCs is heavily dependent on the stability and efficacy of the device's charge transport and light absorption processes. In particular, the perovskite/hole transport layer (HTL) interface at the hole-selective side of PSCs is crucial. To be a suitable hole transport material (HTM), it's valence band maximum (VBM) must be higher than that of perovskite, it should have a high hole mobility to extract holes from the perovskite layer efficiently, and it should form a uniform and compact film when it is processed. 2,2′,7,7′-tetrakis(N,N-di(4-methoxyphenyl)amino)-9,9-spirobifluorene (Spiro-OMeTAD, or in short spiro) is a widely used HTL because it has a suitable alignment between its highest occupied molecular orbital (HOMO) and the valence band of the perovskite light absorbers. This alignment promotes efficient hole extraction from the perovskite material to spiro. Additionally, a conduction band minimum of perovskite material is lower than the lowest unoccupied molecular orbital (LUMO) energy level of spiro, effectively blocking electron transfer from perovskite to spiro. The unique molecular structure of spiro further contributes to its popularity as a HTL [5]. However, the spin-coating process used to manufacture the spiro HTL may lead to the formation of micro- or nanoscale pinholes, which can cause detrimental effects on solar cell performance. These pinholes allow for the diffusion of gases and molecules such as O_2, H_2O, and others, which can react with the perovskite layer and lead to its decomposition. Moreover, the pinholes allow I^- ions to migrate and react with Spiro-OMeTAD$^+$, which reduces the concentration of oxidized Spiro-OMeTAD$^+$ and, in turn, decreases its conductivity [6,7]. Additionally, spiro, on its own, has low hole mobility on the order of 10^{-4} $cm^2V^{-1}s^{-1}$ and smaller hole conductivity than that of

* Corresponding author.
E-mail address: Wenzhi.Li@fiu.edu (W. Li).

https://doi.org/10.1016/j.mtcomm.2023.106846
Received 29 June 2023; Received in revised form 1 August 2023; Accepted 7 August 2023
Available online 9 August 2023

perovskites [8]. To improve its hole mobility and conductivity, lithium bis(trifluoromethylsulfonyl)imide (LiTFSI) is commonly added as a dopant, along with 4-(tert-butyl)pyridine (tBP) to improve solubility [9]. However, incorporating LiTFSI into spiro as a dopant can lead to detrimental effects on PSC's stability. In particular, the hygroscopicity of the LiTFSI salt and its tendency to diffuse into the perovskite film and electron transport layer (ETL), especially under high temperatures, can result in deleterious defects in the perovskite film, leading to increased charge recombination [10].

Recently, inorganic HTMs have gained much attention as potential replacements for spiro HTMs in PSCs due to their remarkable advantages, such as good stability, high abundance, high hole mobility, and low cost. Among these inorganic HTMs, copper-based inorganic p-type semiconductors have been mainly studied for their suitable band alignment with perovskite materials, high conductivity, and chemical stability [11–14]. However, despite their advantages, copper-based HTMs have specific energy levels that result in significant barriers to charge extraction at the interface between the perovskite and copper-based HTLs. This leads to moderate charge collection and enhanced recombination, which can reduce the PSC's efficiency [15]. For instance, Liu et. al. showed that the recombination resistance of perovskite/copper oxide is lower compared to perovskite/spiro, indicating increased recombination losses with inorganic HTL [16]. Further, Tirado et. al. observed a lower V_{OC} when using copper sulfide as the HTL, and the decrease in V_{OC} is attributed to the increased non-radiative recombination at the interface between perovskite and copper sulfide, which is likely influenced by the large energy barrier between their valence bands [17]. To address the issues with existing single-layered HTLs, a novel approach is to make dual HTLs by combining the advantages of organic and inorganic HTMs. This approach has been used in the fabrication of PSCs with different dual HTLs, such as CuSCN/spiro [18], WO_3/spiro [19], NiO_X/spiro [20], $CuInS_2$/spiro [21], which have resulted in improved efficiency and exceptional stability. However, further exploration of dual HTLs is still needed to create highly efficient and stable PSCs.

In this paper, an n-i-p structured methyl ammonium lead iodide ($MAPbI_3$) PSC with a dual-HTL has been simulated using Solar Cell Capacitance Simulator-one Dimension (SCAPS-1D). Dual HTLs consisting of spiro and copper-based HTMs could significantly improve the performance of the PSC. Spiro HTL provides the highest power conversion efficiency (PCE) for PSCs [22] while the addition of copper-based HTL further improves the device's stability and efficiency due to its higher charge carrier mobility, as well as its excellent thermal and chemical stability. Popular copper-based HTLs include copper thiocyanate (CuSCN), copper oxide (Cu_2O), copper iodide (CuI), copper sulfide (CuS), and copper zinc tin sulfide (CZTS) [23]. In this work, various HTL combinations of HTLs such as spiro, Cu_2O/spiro, CuSCN/spiro, spiro/CuI, spiro/CuS, and spiro/CZTS were simulated for PSCs with the ETL (SnO_2) being fixed. Furthermore, the effects of absorber thickness, absorber layer defect density, HTL thickness, absorber/HTL interface defect density, working temperature, series resistance, and shunt resistance on device outcome parameters such as fill factor (FF), short circuit current density (J_{SC}), power conversion efficiency (PCE), and open circuit voltage (V_{OC}) were studied.

2. Methodology

This study used the AM 1.5 G illumination in SCAPS-1D (ver.3.3.10), a simulation software developed by the University of Gent, Belgium [24]. SCAPS-1D uses Poisson's, hole continuity and electron continuity equations to simulate heterostructure solar cells with up to seven layers [25]. Simulation can be conducted both in light and dark environmental conditions.

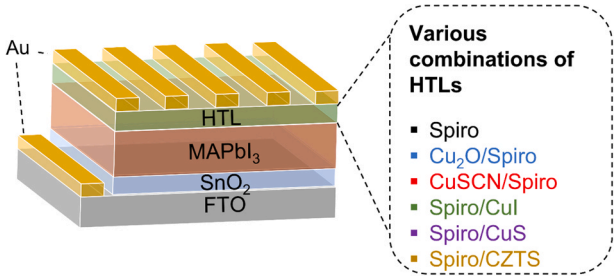

Fig. 1. Device structure of PSC with various combinations of HTLs.

$$\text{Poisson's equation}: -\frac{\partial}{\partial x}\left(-\epsilon(x)\frac{\partial V}{\partial x}\right) = q\left[p(x) - n(x) + N_D^+(x) - N_A^-(x) + p_t(x) - n_t(x)\right]$$

$$\text{Continuity equation for electrons}: \frac{\partial n}{\partial t} = \frac{1}{q}\frac{\partial J_n}{\partial x} + G_n - R_n$$

$$\text{Continuity equation for holes}: \frac{\partial p}{\partial t} = \frac{1}{q}\frac{\partial J_p}{\partial x} + G_p - R_p$$

where, q = charge, ϵ = dielectric permittivity, V= potential, $p(x)$ = concentration of free holes, $n(x)$ = concentration of free electrons, $N_D^+(x)$ = concentration of ionized donor, $N_A^-(x)$ = concentration of ionized acceptor, $p_t(x)$ = hole trap density, $n_t(x)$ = electron trap density, J_n = electron current density, J_p = hole current density, G_n = generation rate of electrons, G_p = generation rate of holes, R_n = electron recombination rate, R_p = hole recombination rate.

The solar cell under investigation comprises a planar n-i-p architecture comprising FTO-coated glass as front contact, SnO_2 as ETL, $MAPbI_3$ as light-absorbing material, different HTMs as HTL, and Au as back contact, as illustrated in Fig. 1. Table 1 gives the basic parameters of each layer of PSCs simulated by SCAPS, where t = thickness, E_g = band gap energy, X = electron affinity, ε = permittivity, N_C = conduction band effective density of states, N_V = valence band effective density of states, v_n = electron thermal velocity, v_p = hole thermal velocity, μ_n = electron mobility, μ_h = hole mobility, N_d = uniform donor density, N_A = uniform acceptor density, and N_t = total defect density. For all the layers, the capture cross-section of electrons and holes is 1E-15 cm^2, the energetic distribution is single, and the reference for defect energy level E_t is above the valence band level (E_V) [26,27]. The work functions of FTO and Au contacts used in the simulation are 4.4 eV and 5.1 eV, respectively [26]. The light illumination is 1000 W/m^2 at AM 1.5 G, the operating temperature is 300 K, and the series and shunt resistances are 5 Ω-cm^2 and 4200 Ω-cm^2, respectively [28]. We simulated a more realistic PSC by including an interface layer between ETL and perovskite and an interface layer between perovskite and HTL. We assumed a neutral defect density of 10^{10} cm^{-3} with an energy level of 0.6 eV above the highest E_V [29].

We modeled and simulated the devices according to the parameters listed in Table 1 and obtained the current density-voltage (J-V) characteristics, as shown in Fig. 2. We observed different J-V characteristics for different PSCs. For $MAPbI_3$-based PSCs, the highest PCE of 23.47 % was achieved when the dual HTL of spiro/CZTS was used in the device, and the device showed an open circuit voltage of V_{OC} = 1.39 V, a short circuit current density of J_{SC} = 22.02 mA/cm^2, and a fill factor of FF = 76.64 %. If spiro along is used as the HTL, the PSC showed a PCE of 21.91 %, V_{OC} = 1.26 V, J_{SC} = 21.92 mA/cm^2, and FF = 79.56 %. For PSCs using CuSCN/spiro, Cu_2O/spiro, spiro/CuI, and spiro/CuS as dual HTLs, PCEs are 14.41 %, 20.73 %, 21.67 %, and 20.44 %, respectively, as shown in Table 2. Additionally, we conducted simulations for PSCs using a single layer of copper-based materials as HTL. The performance parameters is shown in Supplementary file, Table S1. For PSCs

Table 1
Basic parameters of each layer of PSCs that are used in the simulation.

Material Properties	FTO [30]	SnO_2 [25,31]	$MAPbI_3$ [32,33]	Spiro [25]	CZTS [34]	Cu_2O [35,36]	CuI [37–39]	CuSCN [40]	CuS [41]
t (nm)	500	80	500	200	100	100	100	100	100
E_g (eV)	3.5	3.5	1.55	3.0	1.40	2.17	2.98	3.68	2.2
X (eV)	4.0	4.0	3.93	2.45	4.1	3.2	2.1	1.70	2.9
ε	9	9	6.5	3.0	9	7.5	6.5	5.10	10
N_c ($1/cm^3$)	2.2E18	2.2E17	2.2E18	1.2E19	2.2E18	2E18	2.8E19	2.2E20	4.386E19
N_V ($1/cm^3$)	1.8E19	2.2E16	1.8E19	1.8E19	1.8E18	1.1E19	1.8E19	1E20	4.343E19
v_n (cm/s)	10^7	10^7	10^7	10^7	10^7	10^7	10^7	10^7	10^7
v_h (cm/s)	10^7	10^7	10^7	10^7	10^7	10^7	10^7	10^7	10^7
μ_n $cm^2/V.s$	20	20	2	2E-4	100	200	1E2	25	2.5
μ_h $cm^2/V.s$	10	10	2	2E-4	12.5	80	4.39E1	25	2.5
N_D (cm^{-3})	2E19	2.42E19	0	0	0	0	0	0	0
N_A (cm^{-3})	0	0	0	2E18	1E19	2E19	2E19	3E18	1E18
N_t (cm^{-3})	1E15	1E15	2.5E13	1E15	1E15	1E14	1E15	1E15	1E14

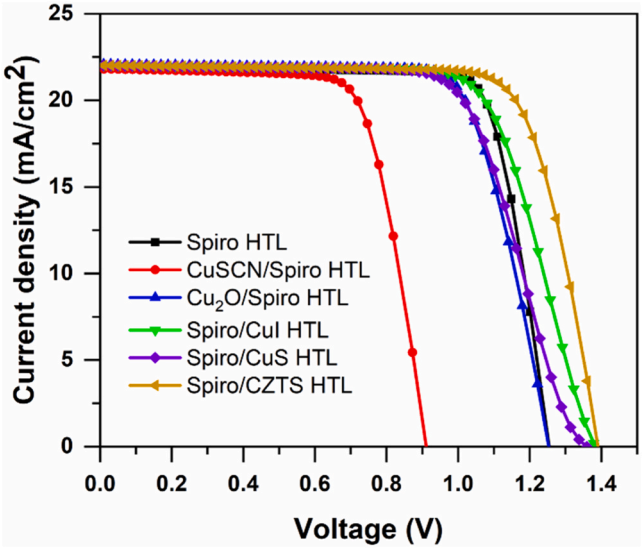

Fig. 2. J-V characteristics of PSCs with various combinations of HTLs.

Table 2
PSCs with various HTLs and their performance parameters.

Device structures	V_{OC} (V)	J_{SC} (mA/cm^2)	FF (%)	PCE (%)
FTO/SnO_2/$MAPbI_3$/ Spiro/Au	1.26	21.92	79.56	21.91
FTO/SnO_2/$MAPbI_3$/CuSCN/Spiro /Au	0.91	21.81	72.43	14.41
FTO/SnO_2/$MAPbI_3$/Cu_2O/Spiro /Au	1.25	22.09	74.88	20.73
FTO/SnO_2/$MAPbI_3$/Spiro/CuI/Au	1.38	22.01	71.12	21.67
FTO/SnO_2/$MAPbI_3$/Spiro/CuS/ Au	1.36	22.02	68.32	20.44
FTO/SnO_2/$MAPbI_3$/Spiro/CZTS/ Au	1.39	22.02	76.64	23.47

employing a single layer of CuI, CuS, and CZTS as HTLs, the PCEs are 19.77 %, 18.37 %, and 20.85 %, respectively. These values are lower than those observed for PSCs with spiro/CuI, spiro/CuS, and spiro/CZTS as HTLs. The reduced PCE can mainly be attributed to the lower V_{OC}. Interestingly, PSCs utilizing CuSCN and Cu_2O as HTLs exhibited slightly higher PCE and FF compared to PSCs with CuSCN/spiro and Cu_2O/spiro as HTLs.

As illustrated in Fig. 2, the J-V curve of the perovskite solar cells using spiro/CuS dual HTLs exhibits a distinctive bend near the V_{OC}, whereas the other cells do not display this characteristic. A bend or an S-shaped J-V curve near V_{OC} typically indicates issues with extracting carriers. This problem is commonly associated with the series resistance of the cell, which can create a charge reservoir at the contact, causing increased recombination within the material [42]. To address this issue, we have explored potential methods to increase the squareness of the J-V curve. By improving the hole mobility of spiro and enhancing the acceptor density of both hole transport materials, we can reduce the bending of the J-V curve near V_{OC} (Supplementary file, Fig. S1).

As shown in Fig. 2, we also observed a significant decrease in the V_{OC} in the CuSCN/spiro HTL-based PSCs compared to other types of cells. Normally, V_{OC} depends on various factors such as band gap, illumination intensity, temperature, exciton generation rate, charge carrier mobility, charge carrier lifetime, and recombination rates [43]. To enhance the performance and V_{OC} of solar cells based on CuSCN/spiro HTL, it is crucial to study the underlying mechanisms behind the lower V_{OC}. This decline could be a result of an increased recombination rate, causing the loss of photogenerated charge carriers. Along with the simulation of recombination rates, we will explore this in the subsequent sections.

3. Results and discussions

3.1. The electric fields at the interfaces of the PSCs with various HTLs combinations

Our simulations of device structures revealed that the electric fields at the interfaces of the constituent layers of the PSCs play an essential role in their operation. The electric fields of the simulated device structures are illustrated in Fig. 3. The electric fields at these devices typically have a negative field at the perovskite/ETL interface and a positive field at the ETL/FTO interface. As shown in Fig. 3(a), at the perovskite/ETL interface, the electric field is directed from the ETL to the perovskite, while at the ETL/FTO interface, the electric field is directed from the ETL to the FTO. At the perovskite/HTL interface, the electric field is directed from the perovskite to the HTL. The electric field at the devices helps to separate the electron-hole pairs, which are generated when the perovskite material absorbs light. The negative electric field near the perovskite/ETL interface encourages the electron to move toward the ETL, while the positive electric field near the ETL/FTO interface can increase the electron recombination rate from the ETL to the FTO electrode. Moreover, we observed a very small peak of a negative electric field at the interface between the perovskite and the spiro HTL (Fig. 3(a)), indicating that it is responsible for transferring photogenerated holes from the perovskite to the HTL. When a dual HTL is used, a significantly large electric field is observed at the interface between the HTL layers. Out of all the HTL combinations, the magnitude of the negative electric field at the interface of the spiro/CZTS HTL is the highest (Fig. 3(f)), suggesting that this HTL combination results in enhanced charge separation and reduced recombination, which could explain the highest PCE (23.47 %) of all HTL combinations, as shown in

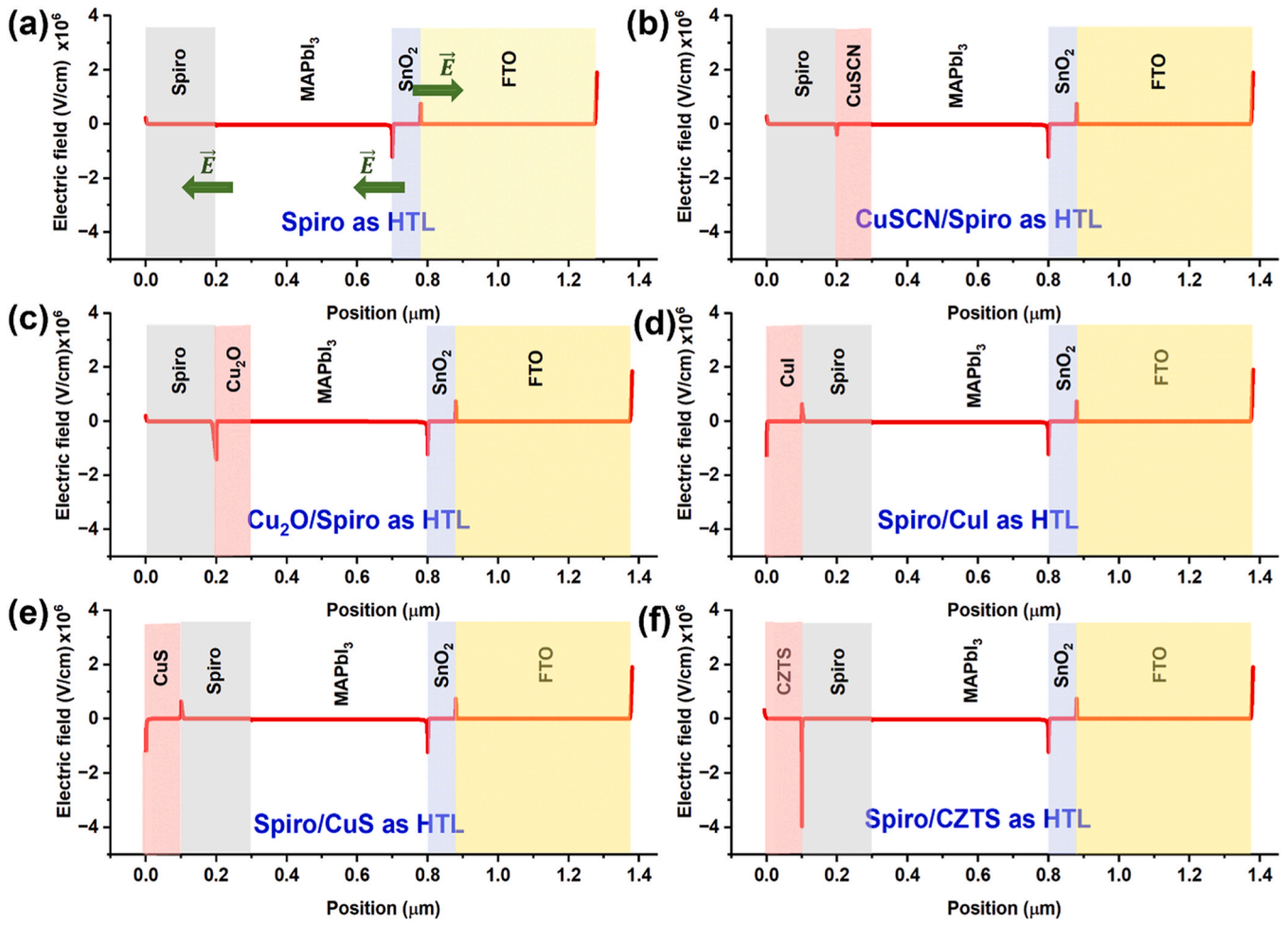

Fig. 3. Electric fields at the interfaces of PSCs with different HTL combinations: (a) Spiro, (b) CuSCN/Spiro, (c) Cu_2O/Spiro, (d) Spiro/CuI, (e) Spiro/CuS, and (f) Spiro/CZTS.

Table 2.

Although the electric field is negative at the CuSCN/spiro (Fig. 3(b)) and Cu_2O/spiro (Fig. 3(c)) interfaces, the electric field strength is relatively small compared to that of the spiro/CZTS interface. At the interfaces of spiro/CuI (Fig. 3(d)) and spiro/CuS (Fig. 3(e)), a positive electric field is presented, which will hinder the carrier collection and increase the recombination.

3.2. Charge recombination in PSCs with various HTL combinations

In this simulation study, we also explored the charge recombination dynamics of PSCs with different HTL combinations (Fig. 4). We found that the recombination rates at the perovskite/ETL interface of PSCs with spiro (Fig. 4(a)), CuSCN/spiro (Fig. 4(b)), and Cu_2O/spiro (Fig. 4 (c)) as HTLs are in the order of 10^{18} $cm^{-3}s^{-1}$, which is considerably higher than the recombination rates at the perovskite/ETL interface of PSCs with spiro/CuI (Fig. 4(d)), spiro/CuS (Fig. 4(e)) and spiro/CZTS (Fig. 4 (f)) as HTLs which are determined to be in the order of 10^{15} $cm^{-3}s^{-1}$. The reduced recombination at the perovskite/ETL interfaces, when spiro/CuI, spiro/CuS, and spiro/CZTS are used as HTLs, is attributed to the increased transport ability of electrons from the perovskite layer to the ETL. Moreover, our simulation results show that the recombination rates at the FTO/ETL interfaces are in the order of 10^{18} $cm^{-3}s^{-1}$ for PSCs with spiro, spiro/CuI, and spiro/CuS, and spiro/CZTS as HTLs, whereas for Cu_2O/spiro and CuSCN/spiro as HTLs, there is a significantly greater recombination rate of 10^{21} $cm^{-3}s^{-1}$. For all device structures, the recombination rate is higher at the FTO/ETL interfaces than at perovskite/ETL interfaces. The higher recombination rate at the FTO/ETL interfaces compared to the recombination rate at the perovskite/ETL interfaces is likely due to the positive electric field generated at the FTO/ETL interfaces (as discussed in Section 3.1), which reduces the transport ability of electrons from the ETL to the FTO and thereby increases the recombination rate at the FTO/ETL interfaces.

Furthermore, we observed a high recombination rate of 10^{19} $cm^{-3}s^{-1}$ at the interface of the perovskite and the HTL for the device with spiro as the HTL. For the devices with dual HTLs, we observed a comparatively lower recombination rate at the perovskite/HTL interface, suggesting a better hole transport ability from the perovskite layer to the HTL. However, we noticed significantly high recombination at the interface of the two HTLs, which are in the order of 10^{20} $cm^{-3}s^{-1}$, 10^{18} $cm^{-3}s^{-1}$, 10^{20} $cm^{-3}s^{-1}$, and 10^{19} $cm^{-3}s^{-1}$, at the interface of CuSCN/spiro, Cu_2O/spiro, spiro/CuI, and spiro/CuS, respectively. The exception is the interface of spiro/CZTS, which has a low recombination rate of 10^{17} $cm^{-3}s^{-1}$. The lower recombination rate at the interface of spiro/CZTS HTLs is attributed to enhanced extraction of holes. For optimal photovoltaic performance, it is essential to efficiently extract holes and minimize recombination at the interface. Additionally, the recombination rate in the absorber layer of PSCs with dual HTLs is lower than in PSCs with spiro as HTL. With spiro as HTL the recombination rate in the absorber layer is in the order of 10^{20} $cm^{-3}s^{-1}$, while the recombination with spiro/CZTS, spiro/CuI, and spiro/CuS have a rate of 10^{16} $cm^{-3}s^{-1}$, CuSCN/spiro of 10^{17} $cm^{-3}s^{-1}$, and Cu_2O/spiro of 10^{18} $cm^{-3}s^{-1}$. The reduction of the recombination rate in the absorber layer for the PSCs with dual HTLs is likely due to the introduction of copper-based HTLs combined with

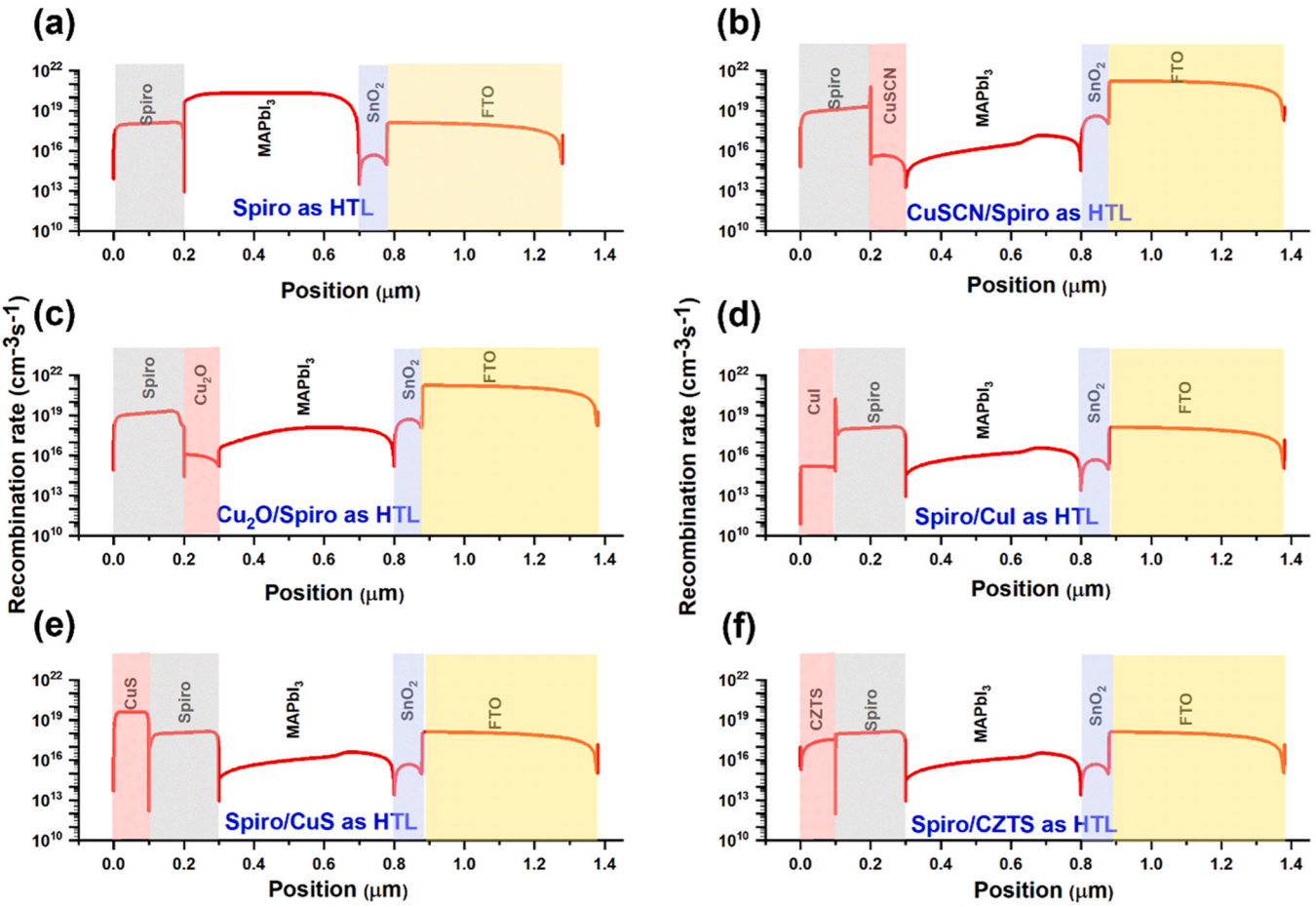

Fig. 4. Charge recombination dynamics of PSCs with different HTL combinations (a) Spiro, (b) CuSCN/Spiro, (c) Cu_2O/Spiro, (d) Spiro/CuI, (e) Spiro/CuS, and (f) Spiro/CZTS.

Table 3
Recombination rates in various layers and interfaces.

	Recombination rate in various layers and interfaces ($cm^{-3}s^{-1}$)								
HTL	FTO	FTO/ETL	ETL	ETL/Perovskite	Perovskite	Perovskite/HTL	Spiro HTL	Cu based HTL	Spiro/Cu based HTL
Spiro	10^{19}	10^{18}	10^{15}	10^{18}	10^{20}	10^{19}	10^{18}	-	-
CuSCN/spiro	10^{21}	10^{21}	10^{18}	10^{18}	10^{17}	10^{14}	10^{19}	10^{15}	10^{20}
Cu_2O/spiro	10^{21}	10^{21}	10^{18}	10^{18}	10^{18}	10^{16}	10^{19}	10^{16}	10^{18}
Spiro/CuI	10^{18}	10^{18}	10^{15}	10^{15}	10^{16}	10^{17}	10^{18}	10^{15}	10^{20}
Spiro/CuS	10^{18}	10^{18}	10^{15}	10^{15}	10^{16}	10^{18}	10^{18}	10^{19}	10^{19}
Spiro/CZTS	10^{18}	10^{18}	10^{15}	10^{15}	10^{16}	10^{18}	10^{18}	10^{17}	10^{17}

spiro-OMeTAD HTLs, which reduces the number of defects in the absorber layer. On the other hand, the ETL layer of the PSCs with CuSCN/spiro and Cu_2O/spiro as HTLs have a higher recombination rate of the order of 10^{18} $cm^{-3}s^{-1}$, which could contribute to the lower PCE of these devices due to increased recombination of charge carriers at the ETL. We observed that when using different HTLs, there are variations in the electron transport abilities between perovskite and the ETL. This can be attributed to not only the impact of the HTL on the concentration of mobile ions and the recombination that occurs at the interface between HTL and perovskite but also the resistance and capacitance of the ETL [44]. Since different HTLs exhibit diverse hole-transporting characteristics, the recombination of photogenerated holes at the interface and bulk of the anodic region alters the bonding state of Pb and I in the perovskite, resulting in differing recombination rates and electron transport ability of photogenerated electrons in the cathodic region. It has been reported that the reactions at the anode region ($2I^- + 2\,h^+ \rightarrow I_2$) and the cathode region ($Pb^{2+} + 2e^- \rightarrow Pb^0$) occur due to change in the bonding state of Pb and I respectively. The reaction caused by the change in bonding state of one region influence the reaction at the other region, and hence influence the recombination rates and transport ability [45]. Furthermore, we did not observe significantly high recombination rate in the HTL except for CuS layer in the spiro/CuS dual HTLs. The high recombination rate of the order of 10^{19} $cm^{-3}s^{-1}$ may be attributed to the positive electric field generated on the spiro/CuS interface, which agrees with our previous assertion of the positive electric field generated on these interfaces. The recombination rates in various layers and interfaces of the PSCs are listed in Table 3. In our comparison of recombination rates across different layers and interfaces, we found that the PSCs with CuSCN/spiro as HTLs exhibited higher recombination rates. This observation may be attributed to the fact that these PSCs had a lower $V_{OC,}$ which is consistent with our descriptions in the previous section.

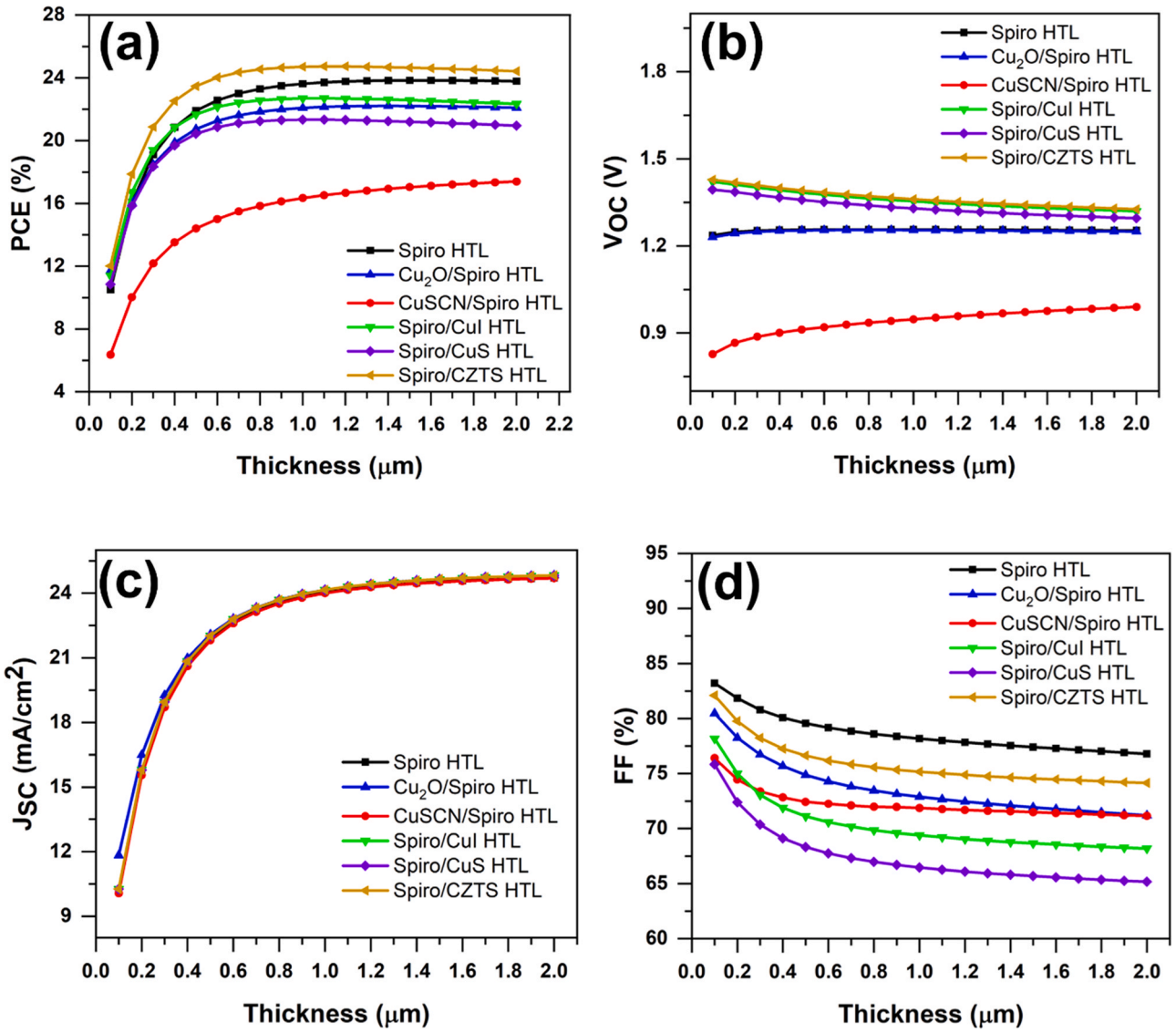

Fig. 5. Effect of the absorber layer thickness on the performance parameters (a) PCE, (b) V_{OC}, (c) J_{SC}, and (d) FF of the PSCs with different HTLs combinations.

3.3. Effect of different parameters on the performance of PSCs with various HTL combinations

3.3.1. Effect of absorber layer thickness

The optimum absorber layer thickness should be determined to achieve the highest PCE of the PSCs. The effect of the absorber layer thickness on the performance parameters of the PSCs with different HTLs is analyzed from 0.1 μm to 2.0 μm (Fig. 5). The PCE of the devices increased rapidly until the absorber layer thickness reached approximately 0.7 μm, beyond which the PCE changed only slightly (Fig. 5(a)). This increase in PCE with the increase in absorber thickness is attributed to the increased J_{SC} (Fig. 5(c)) resulted from increased photon absorption and electron-hole pair generation with increased carrier mobility in the thicker absorber layer. However, for a very thick absorber layer, charge carriers produced inside the absorber layer will recombine if the thickness exceeds the electron diffusion length of absorber material. Hence, the absorber layer should not be too thick. In the simulated thickness range of the absorber layer (0.1–2.0 μm), the PCE and V_{oc} are the highest for the PSCs with spiro/CZTS as HTL (Figs. 5(a) and 5(b)) while the J_{sc} is almost unchanged for the PSC with all the combined HTLs (Fig. 5(c)). In addition, there is no significant change in V_{OC} with the absorber thickness (Fig. 5(b)). The FF (Fig. 5(d)) slightly reduced with the increase of thickness, which suggests the increase of the series resistance of the cell with the absorber layer thickness. Interestingly, when using dual HTL-based PSCs, the FF values are consistently lower in comparison to cells using spiro as HTL. This can be attributed to the addition of a copper-based inorganic layer, which increases the contact resistance between the layers. The higher resistance leads to enhanced interfacial charge recombination and a decrease in FF. Therefore, the device with dual HTLs exhibits a lower FF compared to the device with spiro as the HTL.

3.3.2. Effect of absorber layer defect density

The absorber layer is a critical component of solar cells, where most photovoltaic processes occur. The defect density of the perovskite material affects solar cell performance, so adjusting it to a suitable value is necessary to improve device performance. Defects such as dangling bonds, uncoordinated atoms, surface dislocations, and stoichiometric composition variations can be found at the surface or interface and/or grain boundaries. Bulk defects such as intrinsic point defects, Schottky and Frenkel defects also play a role in altering the properties of the perovskite. A high defect density leads to shorter charge carrier lifetimes and diffusion lengths, increasing recombination and reducing device performance [46]. To achieve perovskite films with low defect density,

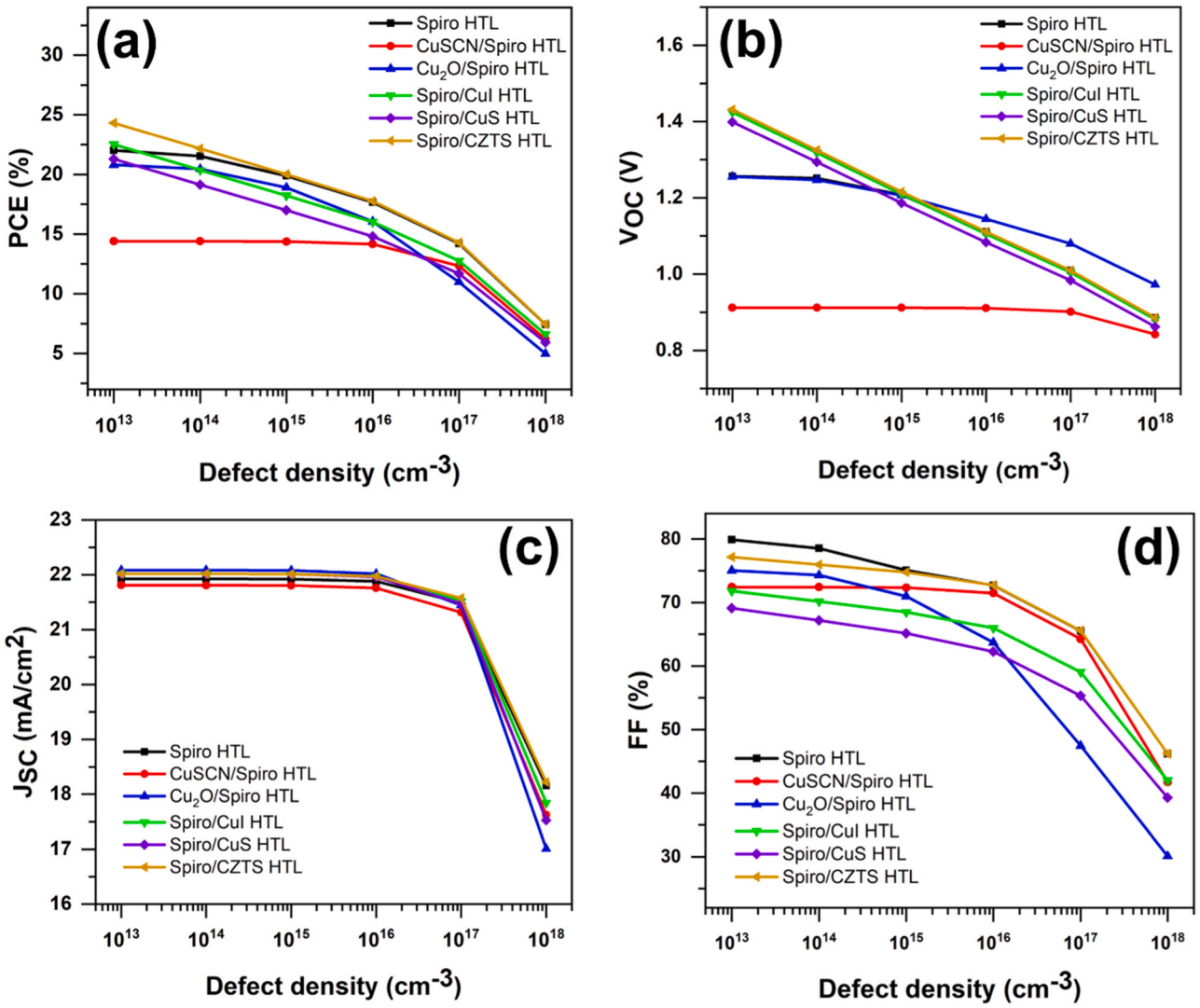

Fig. 6. Effect of the absorber defect density on the performance parameters: (a) PCE, (b) V_{OC}, (c) J_{SC}, and (d) FF of the PSCs with different HTLs combinations.

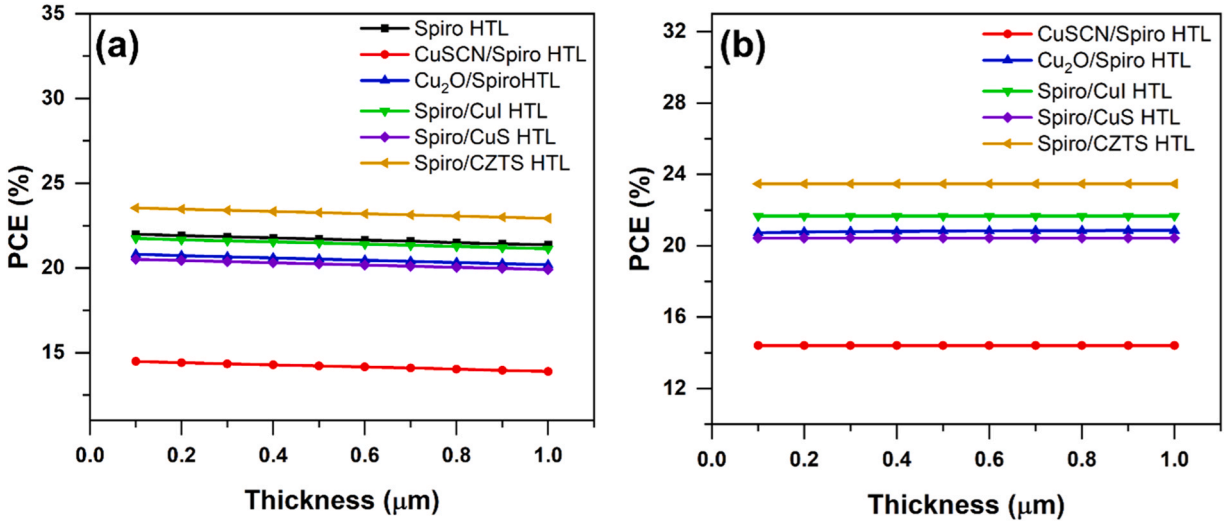

Fig. 7. (a) Effect of spiro thickness variation on the PCE when copper based HTL with constant thickness is used in the dual HTL. (b) Effect of copper based HTL thickness variation on the PCE when spiro with constant thickness is used in the dual HTL.

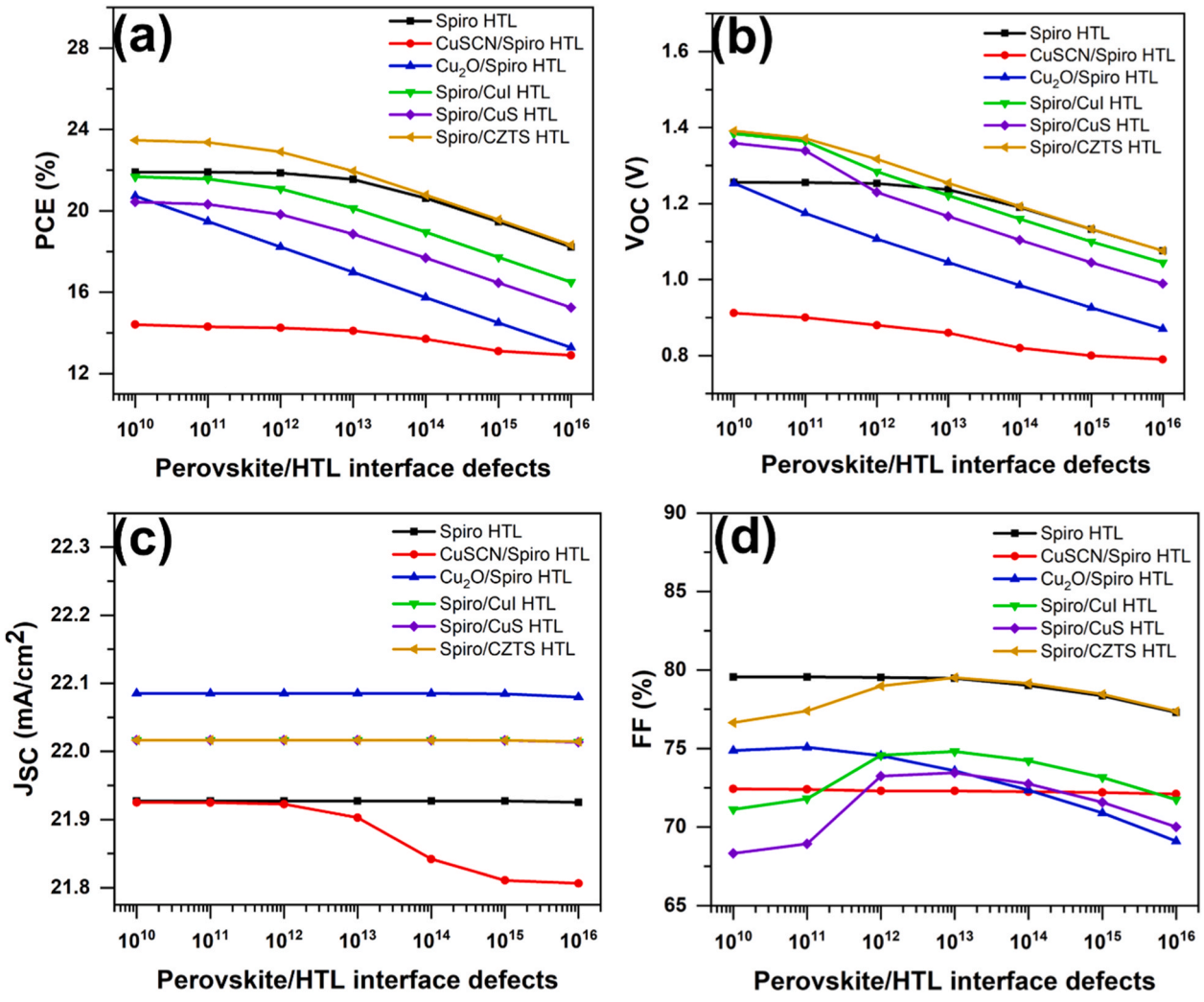

Fig. 8. Effect of the HTL/perovskite interface defect density on the performance parameters (a) PCE, (b) V_{OC}, (c) J_{SC}, and (d) FF of the PSCs with different HTLs combinations.

additives, post-treatment, photochemical curing, large grain sizes, and the formation of single crystalline films are necessary [47]. Simulations can remove defect density, but some defects should be added for a realistic perovskite device. Fig. 6 shows the effect of varying absorber defect density (N_t) on the device parameters. When the N_t values ranged from 10^{13} to 10^{18} cm^{-3}, the V_{OC} decreased (Fig. 6(b)), with the decrease rate being slower for PSCs with Cu_2O/spiro and CuSCN/spiro as HTLs. The decrease rates of J_{SC} (Fig. 6(c)) and FF (Fig. 6(d)) are similar for all HTL combinations. Overall, PCE (Fig. 6(a)) decreased with increasing N_t; however, the reduction in PCE is more rapid after the N_t reaches 10^{17} cm^{-3}. The tolerance of defect density is higher for the PSCs with CuSCN/spiro as HTL than the other HTL combinations. When CuSCN/spiro is used as HTL, the PCE remains constant until the defect density reaches 10^{16} cm^{-3}. When spiro and Cu_2O/spiro are used as HTLs, the PCE remains constant until the defect density is 10^{14} cm^{-3}. The PCE decreases linearly with the increase in defect density for all remaining HTLs (spiro/CuI, spiro/CuS, and spiro/CZTS).

3.3.3. *Effect of HTL thickness*

The thickness of the HTL can be controlled by varying the spin-coating speed when using spin-coating techniques to deposit the layers. Fig. 7(a) shows the PCE change with the spiro layer thickness when the spiro is combined with copper-based HTL of constant thickness, and Fig. 7(b) shows the PCE change with the thickness of a copper-based HTL combined with a spiro layer of constant thickness. We observed a slight reduction in PCE when the thickness of spiro layer increased. This decrease in PCE can be attributed to the decrease in FF (Supplementary file, Fig. S2), which may be associated with the increase in series resistance and reduction of hole mobility with the increase in spiro layer thickness [48]. An optimal spiro layer thickness is necessary to obtain a flat surface without affecting the series resistance of the cell and to maximize hole collection probability, because having an HTL that is either too thin or too thick is not ideal. However, on the other hand, an increase in the thickness of the copper-based HTL did not result in any significant changes in PCE. This may be due to the high charge mobilities and conductivities of copper-based inorganic HTLs compared to the organic spiro HTL [49]. In our simulation study, we found that increasing the thickness of the spiro layer results in a slightly higher increase in resistance compared to increasing the thickness of the inorganic copper-based HTLs.

3.3.4. *Effect of HTL/absorber layer interface defect density*

The presence of chemical impurities, surface dislocations, uncoordinated atoms, and dangling bonds at the surface of perovskite can lead to significant defects at the HTL/absorber layer interface [50]. The defect density significantly impacts the performance of the PSC. These defects act as a recombination center, reducing the efficiency of the PSC by increasing the recombination rate. Fig. 8 illustrates the effects of an increased interface defect density (10^{10} to 10^{16} cm^{-3}) on the performance of PSCs with various HTL combinations (spiro, Cu_2O/spiro,

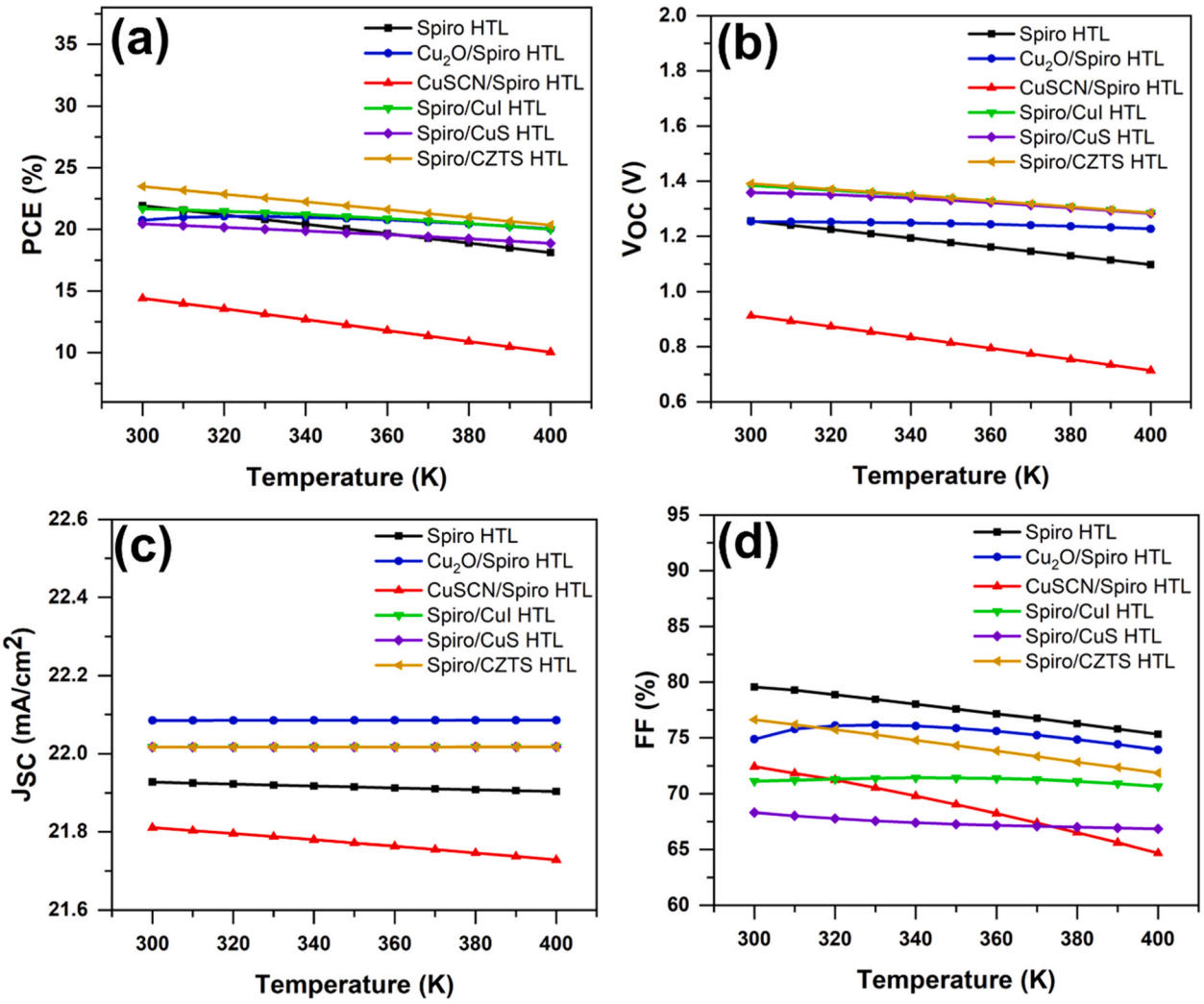

Fig. 9. Effect of the temperature on the performance parameters (a) PCE (b) V_{OC} (c) J_{SC} (d) FF of the PSCs with different HTLs combinations.

spiro/CuI, spiro/CuS, and spiro/CZTS). Fig. 8(a) shows that the PCE decreased significantly with the increased interface defect density for all HTL combinations; the decrease is particularly noticeable beyond 10^{12} cm^{-3} for spiro/CuI, spiro/CuS, and spiro/CZTS. The decrease in PCE is less pronounced for PSCs with CuSCN/spiro as HTL. Interestingly, when spiro is used as HTL, the PCE remained almost the same until the perovskite/HTL interface defect density is 10^{13} cm^{-3}, and only then does it start to decrease. In addition, V_{OC} decreased with the increase of interface defect density for all device structures (Fig. 8(b)), which might be related to increasing carrier recombination. Defects at the interface of the HTL and the perovskite layer can affect the FF of a device (Fig. 8(d)), causing it to fluctuate. Moreover, we did not observe a significant change in J_{SC} values for spiro, Cu_2O/spiro, spiro/CuI, spiro/CuS, and spiro/CZTS with the HTL/perovskite interface defect density in the range of 10^{10} to 10^{16} cm^{-3} (Fig. 8(c)). Interestingly, for the PSC with CuSCN/spiro as HTL, J_{SC} started to decrease slightly after 10^{13} cm^{-3}. This decrease can be attributed to incomplete hole collection at the interface between the perovskite layer and the HTL. When the defect density at the $MAPbI_3$/CuSCN interface exceeds 10^{13} cm^{-3}, the holes traveling from the $MAPbI_3$ absorber layer to the CuSCN HTL are more likely to get trapped, scattered, or recombined, leading to incomplete hole collection. Moreover, the simulation showed that the FF and V_{OC} of PSCs with CuSCN/spiro as the HTL did not change significantly compared to that of PSCs with other HTL combinations.

3.3.5. *Effect of temperature*

To better understand how PSCs with different HTL combinations perform in various environmental conditions, particularly at higher temperatures, which is especially important for space applications, we measured the performance of the devices at temperatures ranging from 300 to 400 K. Fig. 9 shows the variation of device parameters with temperature. As shown in Fig. 9(b), V_{OC} decreased significantly with the increase in temperature for all PSCs except those with Cu_2O/spiro as HTL, which showed only a slight decrease. The decrease in V_{OC} is attributed to increased saturation current due to a shift in intrinsic carrier concentrations when the temperature rises, leading to higher recombination rates [51]. Furthermore, the temperature increase has a negligible effect on the J_{SC} of all PSCs (Fig. 9(c)), except for the device with CuSCN/spiro as the HTL, which see a decrease. Fig. 9(d) demonstrated that the FF decreased for all devices except for the device utilizing Cu_2O/spiro HTL. In the case of Cu_2O/spiro as the HTL, the FF experienced a slight increase until the temperature reached 330 K. However, beyond this temperature, the FF began to decrease. This could be attributed to the high carrier mobilities of Cu_2O, which influence the conductivity of the Cu_2O layer and consequently reduce the series resistance of the cells. The reduced series resistance allowed PSCs with Cu_2O/spiro as HTL to withstand the interfacial defects caused by increasing temperatures up to 330 K. However, beyond this threshold, the deformation stress on the layers may increase causing interfacial defects. Consequently, the series resistance increased, resulting in a

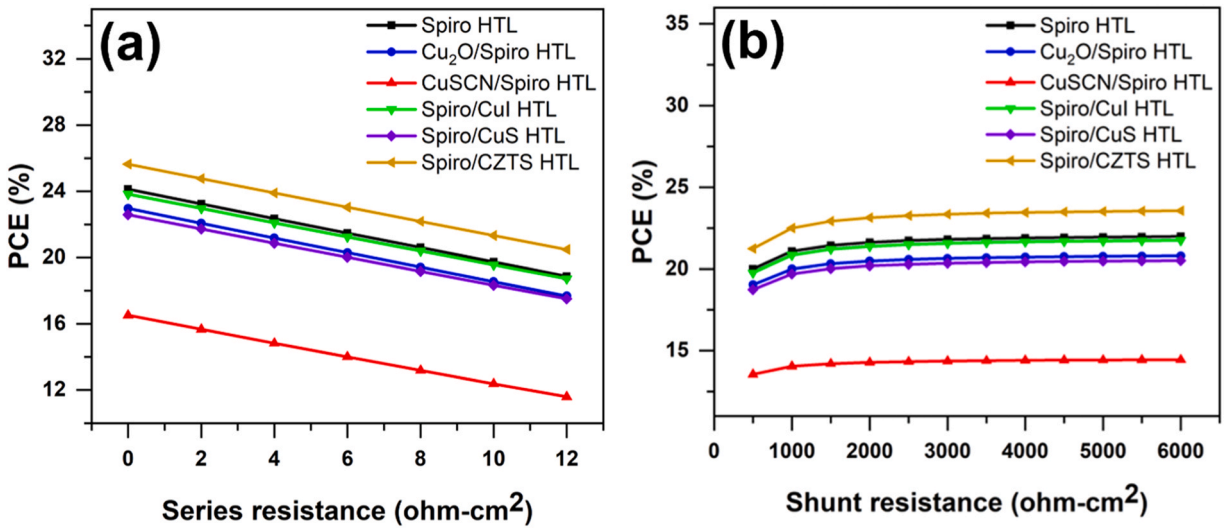

Fig. 10. Effect of the (a) series resistance and (b) shunt resistance on the performance of the PSCs with different HTLs combinations.

reduced FF [52]. Overall, Fig. 9(a) showed that PCE decreased with the increase in temperature. Of all the device structures, the PSC with Cu_2O/spiro HTL is more resistant to temperature increase. It has a PCE of 20.73 % at 300 K. This PCE increased to 21.03 % at 330 K before decreasing to 20.03 % at 400 K.

3.3.6. *Effect of series and shunt resistances*

The series resistance (Rs) of a solar cell is determined by various factors, including the electrical resistance of the contacts (FTO and gold) and the resistance of the ETL, HTL, and active layers. The resistance of the contacts is influenced by the material's work function and the thickness of the layer. Furthermore, electrons can be lost due to scattering and recombination with holes within the ETL, HTL, and perovskite layers, thus contributing to the device's overall resistance. Hence, it is essential to reduce the series resistance to maximize the efficiency of PSCs. This can be accomplished by doping suitable chemicals into the charge transport and perovskite layers, applying appropriate interface modifiers, optimizing fabrication techniques, etc. [53]. These methods have been successfully used to reduce the series resistance and improve the performance of PSCs. Fig. 10(a) illustrates the effects of series resistance (R_s) in the range of 0–12 Ω-cm^2 on the performance of PSCs with various HTL combinations, while the shunt resistance (R_{SH}) is kept constant at 4200 Ω-cm^2. The PCE (Fig. 10(a)) decreased significantly with the increment in R_S for each device. We observed a linear decrease in PCE with increased series resistance. When the series resistance increased from 0 ohm-cm^2 to 12 ohm-cm^2, the most remarkable drop in PCE is observed for the PSC with CuSCN/spiro as the HTL, which is only able to retain 70.19 % of its initial PCE. On the other hand, the smallest drop in PCE is observed for the PSC with spiro/CZTS as the HTL, which is able to retain 79.87 % of its initial PCE. For spiro, Cu_2O/spiro, spiro/CuI, and spiro/Cus as HTLs, the corresponding retained percentages of PCE are 78.20 %, 77 %, 78.56 %, and 77.52 %, respectively.

We further studied the effect of shunt resistance on the performance of PSCs by simulating the device's performance when the shunt resistance is varied from 500 Ω-cm^2 to 6000 Ω-cm^2 and series resistance is kept constant at 5 Ω-cm^2. A higher shunt resistance value is essential for better device performance, as a low value diverts current to an alternative path and reduces the current flowing through the junction. As we increased the shunt resistance for the PSCs, PCE (Fig. 10(b)) remained constant beyond 1000 Ω-cm^2 for all different HTL combinations.

From the simulation, we observed that devices with low series resistance and high shunt resistance gave better performance. Furthermore, devices with spiro/CZTS as the HTL are more tolerant to increases in series resistance. In addition, we did not observe any interesting results from the variation of shunt resistance.

4. Conclusion

The present research studied the possibility of synthesizing PSCs with a combination of both organic and inorganic HTMs. The performance of $MAPbI_3$ PSCs with dual HTLs (Cu_2O/spiro, CuSCN/spiro, spiro/CuI, spiro/CuS, spiro/CZTS) was simulated and compared to that of a conventional device with spiro as HTL. The highest efficiency was obtained for the PSC with spiro/CZTS as HTL. This result is attributed to better charge extraction and reduced recombination at the interface and in the device, respectively. Furthermore, the PCE increased with the increase in absorber thickness and decreased with the increase in absorber defect density. Changes in HTL thickness had no effect on the PCE. PCE decreased with the increase in HTL/perovskite interface defect for all the studied device structures. Generally, PCE decreased with the increase in temperature; however, the PSC with Cu_2O/spiro as HTL had more resistance to the temperature increase. Simulation of the device also showed that the PCE decreased with the increase in series resistance and increased with the increase in shunt resistance up to a certain point.

Author Agreement Statement

We the undersigned declare that this manuscript is original, has not been published before and is not currently being considered for publication elsewhere. We confirm that the manuscript has been read and approved by all named authors and that there are no other persons who satisfied the criteria for authorship but are not listed. We further confirm that the order of authors listed in the manuscript has been approved by all of us. We understand that the Corresponding Author is the sole contact for the Editorial process. He/she is responsible for communicating with the other authors about progress, submissions of revisions and final approval of proofs.

Declaration of Competing Interest

The authors declare that they have no known competing financial interests or personal relationships that could have appeared to influence the work reported in this paper.

Data Availability

Data will be made available on request.

Acknowledgment

This work was supported by the National Science Foundation under grants 1506640 and 2213923.

Appendix A. Supporting information

Supplementary data associated with this article can be found in the online version at doi:10.1016/j.mtcomm.2023.106846.

References

[1] T. Baikie, Y. Fang, J.M. Kadro, M. Schreyer, F. Wei, S.G. Mhaisalkar, M. Graetzel, T. J. White, Synthesis and crystal chemistry of the hybrid perovskite (CH3NH3)PbI3 for solid-state sensitised solar cell applications, J. Mater. Chem. A Mater. 1 (2013) 5628–5641, https://doi.org/10.1039/C3TA10518K.

[2] B. Saparov, D.B. Mitzi, Organic–inorganic perovskites: structural versatility for functional materials design, Chem. Rev. 116 (2016) 4558–4596, https://doi.org/10.1021/acs.chemrev.5b00715.

[3] S.D. Stranks, G.E. Eperon, G. Grancini, C. Menelaou, M.J.P. Alcocer, T. Leijtens, L. M. Herz, A. Petrozza, H.J. Snaith, Electron-hole diffusion lengths exceeding 1 micrometer in an organometal trihalide perovskite absorber, Science 342 (2013) (1979) 341, https://doi.org/10.1126/science.1243982.

[4] B. Dahal, W. Li, Configuration of methylammonium lead iodide perovskite solar cell and its effect on the device's performance: a review, Adv. Mater. Interfaces 9 (2022), 2200042, https://doi.org/10.1002/admi.202200042.

[5] G.-W. Kim, H. Choi, M. Kim, J. Lee, S.Y. Son, T. Park, Hole transport materials in conventional structural (n–i–p) perovskite solar cells: from past to the future, Adv. Energy Mater. 10 (2020), 1903403, https://doi.org/10.1002/aenm.201903403.

[6] Q. Wang, Z. Lin, J. Su, Z. Hu, J. Chang, Y. Hao, Recent progress of inorganic hole transport materials for efficient and stable perovskite solar cells, Nano Sel. 2 (2021) 1055–1080, https://doi.org/10.1002/nano.202000238.

[7] J. Carrillo, A. Guerrero, S. Rahimnejad, O. Almora, I. Zarazua, E. Mas-Marza, J. Bisquert, G. Garcia-Belmonte, Ionic reactivity at contacts and aging of methylammonium lead triiodide perovskite solar cells, Adv. Energy Mater. 6 (2016), 1502246, https://doi.org/10.1002/aenm.201502246.

[8] Y. Shen, K. Deng, L. Li, Spiro-OMeTAD-based hole transport layer engineering toward stable perovskite solar cells, Small Methods 6 (2022), 2200757, https://doi.org/10.1002/smtd.202200757.

[9] G. Ren, W. Han, Y. Deng, W. Wu, Z. Li, J. Guo, H. Bao, C. Liu, W. Guo, Strategies of modifying spiro-OMeTAD materials for perovskite solar cells: a review, J. Mater. Chem. A Mater. 9 (2021) 4589–4625, https://doi.org/10.1039/D0TA11564A.

[10] Y. Shen, K. Deng, L. Li, Spiro-OMeTAD-based hole transport layer engineering toward stable perovskite solar cells, Small Methods 6 (2022), 2200757, https://doi.org/10.1002/smtd.202200757.

[11] Q. Wu, C. Xue, Y. Li, P. Zhou, W. Liu, J. Zhu, S. Dai, C. Zhu, S. Yang, Kesterite Cu2ZnSnS4 as a low-cost inorganic hole-transporting material for high-efficiency perovskite solar cells, ACS Appl. Mater. Interfaces 7 (2015) 28466–28473, https://doi.org/10.1021/acsami.5b09572.

[12] W. Yu, F. Li, H. Wang, E. Alarousu, Y. Chen, B. Lin, L. Wang, M.N. Hedhili, Y. Li, K. Wu, X. Wang, O.F. Mohammed, T. Wu, Ultrathin Cu2O as an efficient inorganic hole transporting material for perovskite solar cells, Nanoscale 8 (2016) 6173–6179, https://doi.org/10.1039/c5nr07758c.

[13] V.E. Madhavan, I. Zimmermann, C. Roldán-Carmona, G. Grancini, M. Buffiere, A. Belaidi, M.K. Nazeeruddin, Copper thiocyanate inorganic hole-transporting material for high-efficiency perovskite solar cells, ACS Energy Lett. 1 (2016) 1112–1117, https://doi.org/10.1021/acsenergylett.6b00501.

[14] P. Nazari, F. Ansari, B. Abdollahi Nejand, V. Ahmadi, M. Payandeh, M. Salavati-Niasari, Physicochemical interface engineering of CuI/Cu as advanced potential hole-transporting materials/metal contact couples in hysteresis-free ultralow-cost and large-area perovskite solar cells, J. Phys. Chem. C. 121 (2017) 21935–21944, https://doi.org/10.1021/acs.jpcc.7b07061.

[15] J. Tsiba Matondo, D. Malouangou Maurice, Q. Chen, L. Bai, M. Guli, Inorganic copper-based hole transport materials for perovskite photovoltaics: Challenges in normally structured cells, advances in photovoltaic performance and device stability, Sol. Energy Mater. Sol. Cells 224 (2021), 111011, https://doi.org/10.1016/j.solmat.2021.111011.

[16] C. Liu, X. Zhou, S. Chen, X. Zhao, S. Dai, B. Xu, Hydrophobic Cu2O quantum dots enabled by surfactant modification as top hole-transport materials for efficient perovskite solar cells, Adv. Sci. 6 (2019), 1801169, https://doi.org/10.1002/advs.201801169.

[17] J. Tirado, C. Roldán-Carmona, F.A. Muñoz-Guerrero, G. Bonilla-Arboleda, M. Ralaiarisoa, G. Grancini, V.I.E. Queloz, N. Koch, M.K. Nazeeruddin, F. Jaramillo, Copper sulfide nanoparticles as hole-transporting-material in a fully-inorganic blocking layers n-i-p perovskite solar cells: application and working insights, Appl. Surf. Sci. 478 (2019) 607–614, https://doi.org/10.1016/j.apsusc.2019.01.289.

[18] Q. Li, Y. Zhao, R. Fu, W. Zhou, Y. Zhao, F. Lin, S. Liu, D. Yu, Q. Zhao, Enhanced long-term stability of perovskite solar cells using a double-layer hole transport material, J. Mater. Chem. A Mater. 5 (2017) 14881–14886, https://doi.org/10.1039/C7TA03315J.

[19] G.-W. Kim, G. Kang, K. Choi, H. Choi, T. Park, Solution processable inorganic–organic double-layered hole transport layer for highly stable planar perovskite solar cells, Adv. Energy Mater. 8 (2018), 1801386, https://doi.org/10.1002/aenm.201801386.

[20] R. Li, P. Wang, B. Chen, X. Cui, Y. Ding, Y. Li, D. Zhang, Y. Zhao, X. Zhang, NiOx/Spiro hole transport bilayers for stable perovskite solar cells with efficiency exceeding 21%, ACS Energy Lett. 5 (2020) 79–86, https://doi.org/10.1021/acsenergylett.9b02112.

[21] Q. Zhou, W. Ma, Z. Zhang, Y. Liu, H. Zhang, Y. Mao, Double-layered hole transport material of CuInS2/Spiro for highly efficient and stable perovskite solar cells, Org. Electron 96 (2021), 106249, https://doi.org/10.1016/j.orgel.2021.106249.

[22] M. Kim, J. Jeong, H. Lu, T.K. Lee, F.T. Eickemeyer, Y. Liu, I.W. Choi, S.J. Choi, Y. Jo, H.-B. Kim, S.-I. Mo, Y.-K. Kim, H. Lee, N.G. An, S. Cho, W.R. Tress, S. M. Zakeeruddin, A. Hagfeldt, J.Y. Kim, M. Grätzel, D.S. Kim, Conformal quantum dot–SnO2 layers as electron transporters for efficient perovskite solar cells, Science 375 (2022) (1979) 302–306, https://doi.org/10.1126/science.abh1885.

[23] J. Tsiba Matondo, D. Malouangou Maurice, Q. Chen, L. Bai, M. Guli, Inorganic copper-based hole transport materials for perovskite photovoltaics: Challenges in normally structured cells, advances in photovoltaic performance and device stability, Sol. Energy Mater. Sol. Cells 224 (2021), 111011, https://doi.org/10.1016/j.solmat.2021.111011.

[24] M. Burgelman, P. Nollet, S. Degrave, Modelling polycrystalline semiconductor solar cells, Thin Solid Films 361–362 (2000) 527–532, https://doi.org/10.1016/S0040-6090(99)00825-1.

[25] F. Azri, A. Meftah, N. Sengouga, A. Meftah, Electron and hole transport layers optimization by numerical simulation of a perovskite solar cell, Sol. Energy 181 (2019) 372–378, https://doi.org/10.1016/j.solener.2019.02.017.

[26] S. Tariq Jan, M. Noman, Influence of layer thickness, defect density, doping concentration, interface defects, work function, working temperature and reflecting coating on lead-free perovskite solar cell, Sol. Energy 237 (2022) 29–43, https://doi.org/10.1016/j.solener.2022.03.069.

[27] S. Sarker, M.T. Islam, A. Rauf, H. Al Jame, Md.R. Jani, S. Ahsan, Md.S. Islam, S. S. Nishat, K.Md Shorowordi, S. Ahmed, A SCAPS simulation investigation of non-toxic MAGeI3-on-Si tandem solar device utilizing monolithically integrated (2-T) and mechanically stacked (4-T) configurations, Sol. Energy 225 (2021) 471–485, https://doi.org/10.1016/j.solener.2021.07.057.

[28] T. Ouslimane, L. Et-taya, L. Elmaimouni, A. Benami, Impact of absorber layer thickness, defect density, and operating temperature on the performance of MAPbI3 solar cells based on ZnO electron transporting material, Heliyon 7 (2021), e06379, https://doi.org/10.1016/j.heliyon.2021.e06379.

[29] S.Z. Haider, H. Anwar, S. Manzoor, A.G. Ismail, M. Wang, A theoretical study for high-performance inverted p-i-n architecture perovskite solar cells with cuprous iodide as hole transport material, Curr. Appl. Phys. 20 (2020) 1080–1089, https://doi.org/10.1016/j.cap.2020.06.022.

[30] S. Abdelaziz, A. Zekry, A. Shaker, M. Abouelatta, Investigating the performance of formamidinium tin-based perovskite solar cell by SCAPS device simulation, Opt. Mater. (Amst.) 101 (2020), 109738, https://doi.org/10.1016/j.optmat.2020.109738.

[31] M.K. Otoufi, M. Ranjbar, A. Kermanpur, N. Taghavinia, M. Minbashi, M. Forouzandeh, F. Ebadi, Enhanced performance of planar perovskite solar cells using TiO2/SnO2 and TiO2/WO3 bilayer structures: roles of the interfacial layers, Sol. Energy 208 (2020) 697–707, https://doi.org/10.1016/j.solener.2020.08.035.

[32] M. Belarbi, O. Zeggai, S. Louhibi-Fasla, Numerical study of methylammonium lead iodide perovskite solar cells using SCAPS-1D simulation program, Mater. Today Proc. 51 (2022) 2115–2119, https://doi.org/10.1016/j.matpr.2021.12.425.

[33] Y. Raoui, H. Ez-Zahraouy, N. Tahiri, O. El Bounagui, S. Ahmad, S. Kazim, Performance analysis of MAPbI3 based perovskite solar cells employing diverse charge selective contacts: simulation study, Sol. Energy 193 (2019) 948–955, https://doi.org/10.1016/j.solener.2019.10.009.

[34] A.C. Piñón Reyes, R.C. Ambrosio Lázaro, K. Monfil Leyva, J.A. Luna López, J. Flores Méndez, A.H. Heredia Jiménez, A.L. Muñoz Zurita, F. Severiano Carrillo, E. Ojeda Durán, Study of a lead-free perovskite solar cell using CZTS as HTL to Achieve a 20% PCE by SCAPS-1D simulation, Micro (Basel) 12 (2021), https://doi.org/10.3390/mi12121508.

[35] A. Tara, V. Bharti, S. Sharma, R. Gupta, Computational approach to explore suitable charge transport layers for all inorganic CsGeI3 perovskite solar cells, Opt. Mater. (Amst.) 128 (2022), 112403, https://doi.org/10.1016/j.optmat.2022.112403.

[36] D.A. Fentahun, A. Tyagi, K.K. Kar, Numerically investigating the AZO/Cu2O heterojunction solar cell using ZnO/CdS buffer layer, Optik (Stuttg) 228 (2021), 166228, https://doi.org/10.1016/j.ijleo.2020.166228.

[37] MostM. Khatun, A. Sunny, S.R. al Ahmed, Numerical investigation on performance improvement of WS2 thin-film solar cell with copper iodide as hole transport layer, Sol. Energy 224 (2021) 956–965, https://doi.org/10.1016/j.solener.2021.06.062.

[38] M.M. Salah, K.M. Hassan, M. Abouelatta, A. Shaker, A comparative study of different ETMs in perovskite solar cell with inorganic copper iodide as HTM, Optik (Stuttg) 178 (2019) 958–963, https://doi.org/10.1016/j.ijleo.2018.10.052.

[39] A.K. Singh, S. Srivastava, A. Mahapatra, J.K. Baral, B. Pradhan, Performance optimization of lead free-MASnI3 based solar cell with 27% efficiency by numerical simulation, Opt. Mater. (Amst.) 117 (2021), 111193, https://doi.org/10.1016/j.optmat.2021.111193.

[40] Md.D. Haque, Md.H. Ali, A.Z.Md.T. Islam, Efficiency enhancement of WSe2 heterojunction solar cell with CuSCN as a hole transport layer: a numerical simulation approach, Sol. Energy 230 (2021) 528–537, https://doi.org/10.1016/j.solener.2021.10.054.

[41] H. Abnavi, D.K. Maram, A. Abnavi, Performance analysis of several electron/hole transport layers in thin film MAPbI3-based perovskite solar cells: a simulation study, Opt. Mater. (Amst.) 118 (2021), 111258, https://doi.org/10.1016/j.optmat.2021.111258.
[42] A. Sundqvist, O.J. Sandberg, M. Nyman, J.-H. Smått, R. Österbacka, Origin of the S-Shaped JV curve and the light-soaking issue in inverted organic solar cells, Adv. Energy Mater. 6 (2016), 1502265, https://doi.org/10.1002/aenm.201502265.
[43] N.K. Elumalai, A. Uddin, Open circuit voltage of organic solar cells: an in-depth review, Energy Environ. Sci. 9 (2016) 391–410, https://doi.org/10.1039/C5EE02871J.
[44] I.M. Hermes, Y. Hou, V.W. Bergmann, C.J. Brabec, S.A.L. Weber, The interplay of contact layers: how the electron transport layer influences interfacial recombination and hole extraction in perovskite solar cells, J. Phys. Chem. Lett. 9 (2018) 6249–6256, https://doi.org/10.1021/acs.jpclett.8b02824.
[45] T. Sekimoto, T. Matsui, T. Nishihara, R. Uchida, T. Sekiguchi, T. Negami, Influence of a hole-transport layer on light-induced degradation of mixed organic–inorganic halide perovskite solar cells, ACS Appl. Energy Mater. 2 (2019) 5039–5049, https://doi.org/10.1021/acsaem.9b00709.
[46] S. Karthick, S. Velumani, J. Bouclé, Chalcogenide BaZrS3 perovskite solar cells: a numerical simulation and analysis using SCAPS-1D, Opt. Mater. (Amst.) 126 (2022), 112250, https://doi.org/10.1016/j.optmat.2022.112250.
[47] F. Wang, S. Bai, W. Tress, A. Hagfeldt, F. Gao, Defects engineering for high-performance perovskite solar cells, NPJ Flex. Electron. 2 (2018) 22, https://doi.org/10.1038/s41528-018-0035-z.
[48] A. Bag, R. Radhakrishnan, R. Nekovei, R. Jeyakumar, Effect of absorber layer, hole transport layer thicknesses, and its doping density on the performance of perovskite solar cells by device simulation, Sol. Energy 196 (2020) 177–182, https://doi.org/10.1016/j.solener.2019.12.014.
[49] G. Pindolia, S.M. Shinde, P.K. Jha, Optimization of an inorganic lead free RbGeI3 based perovskite solar cell by SCAPS-1D simulation, Sol. Energy 236 (2022) 802–821, https://doi.org/10.1016/j.solener.2022.03.053.
[50] Md.M. Haque, S. Mahjabin, S. Khan, M.I. Hossain, G. Muhammad, Md Shahiduzzaman, K. Sopian, Md Akhtaruzzaman, Study on the interface defects of eco-friendly perovskite solar cells, Sol. Energy 247 (2022) 96–108, https://doi.org/10.1016/j.solener.2022.10.024.
[51] G. Pindolia, S.M. Shinde, P.K. Jha, Optimization of an inorganic lead free RbGeI3 based perovskite solar cell by SCAPS-1D simulation, Sol. Energy 236 (2022) 802–821, https://doi.org/10.1016/j.solener.2022.03.053.
[52] S. Yasin, T. Al Zoubi, M. Moustafa, Design and simulation of high efficiency lead-free heterostructure perovskite solar cell using SCAPS-1D, Optik (Stuttg) 229 (2021), 166258, https://doi.org/10.1016/j.ijleo.2021.166258.
[53] S. Ghosh, S. Porwal, T. Singh, Investigation of the role of back contact work function for hole transporting layer free perovskite solar cells applications, Optik (Stuttg) 256 (2022), 168749, https://doi.org/10.1016/j.ijleo.2022.168749.